PERGAMON

AE International – Asia

Atmospheric Environment 37 (2003) 2463–2475

ATMOSPHERIC ENVIRONMENT

www.elsevier.com/locate/atmosenv

Solar actinic flux and photolysis frequency determinations by radiometers and a radiative transfer model at Rishiri Island: comparisons, cloud effects, and detection of an aerosol plume from Russian forest fires

Yugo Kanaya[a,*], Yoshizumi Kajii[b], Hajime Akimoto[a]

[a] *Atmospheric Composition Research Program, Frontier Research System for Global Change, 3173-25 Showa-machi, Kanazawa-ku, Yokohama, Japan*

[b] *Department of Applied Chemistry, Graduate School of Engineering, Tokyo Metropolitan University, Hachioji, Japan*

Received 10 October 2002; accepted 5 March 2003

Abstract

A spectroradiometer equipped with a single monochromator/diode array detector and a $J(NO_2)$ filter radiometer (both from Meteorologie Consult, GmbH) were deployed at Rishiri Island in June 2000 to determine spectral actinic fluxes and photolysis frequencies of atmospheric chemical species. The measured 2π-sr actinic fluxes for the 320–700 nm wavelength region under clear conditions closely agreed with those calculated by using the TUV radiative transfer model especially with small solar zenith angles ($<60^\circ$), while the pixels of the diode array for 295–305 nm suffered from a stray light problem and resulted in overestimation. J values of more than 20 chemical species of atmospheric interest including those of NO_2 and halogenated species were calculated by convoluting the absorption cross sections and quantum yields with the observed actinic fluxes. The $J(NO_2)$ values agreed very well with the 2π component of the $J(NO_2)$ values from the filter radiometer even under cloudy conditions. Each J value under clear conditions was approximated by using three parameters. The effects of clouds and aerosols on actinic fluxes were studied as functions of wavelength. The presence of clouds attenuated actinic fluxes at longer wavelengths more efficiently, but the transmission factor was almost constant throughout 320–700 nm. During 3 days, an aerosol plume presumably originating from Russian forest fires heavily attenuated actinic fluxes in the UV region.

Keywords: Actinic flux; $J(NO_2)$; Halogenated species; Aerosols; Forest fire

1. Introduction

In the troposphere, it has been widely recognized that the OH radical is a key component that reacts with many trace gases, such as NO_x, CO, and hydrocarbons, and determines their residence time in the atmosphere. HO_2 radical, NO, and NO_2 are also important trace gases in producing and reducing tropospheric ozone through photochemistry, which is a toxic gas for biota and one of the most important greenhouse gases. The OH and HO_2 radicals are initially produced by the photolyses of ozone, aldehydes, and peroxides, while NO/NO_2 balance is controlled by the photolysis of NO_2 by sunlight. Thus the precise determination of these photolysis frequencies, called J values, is essential to quantitative understanding of fast photochemistry in the troposphere.

There are three major techniques to measure J values (Lantz et al., 1996; Shetter et al., 1996; Hofzumahaus et al., 1999): The first one is the chemical actinometry. In the technique, flowing or static gas containing the

*Corresponding author. Tel.: +81-45-778-5720.
E-mail address: yugo@jamstec.go.jp (Y. Kanaya).

1352-2310/03/$ - see front matter
doi:10.1016/S1352-2310(03)00183-3

chemical compound whose J value is to be measured is exposed to sunlight and the chemical product due to the photolysis or its derivative is measured (Kelley et al., 1995; Shetter et al., 1996; Kraus et al., 2000). The second technique is the spectroradiometry, where the solar actinic flux, $F(\lambda)$, is first measured as a function of wavelength which is then convoluted with the absorption cross section ($\sigma_i(\lambda)$) and the quantum yield for dissociation ($\phi_i(\lambda)$) of a chemical species of interest, i, to produce its J value:

$$J_i = \int F(\lambda)\,\sigma_i(\lambda)\,\phi_i(\lambda)\,\mathrm{d}\lambda. \quad (1)$$

J values of various chemical species can be calculated from the flux data if $\sigma_i(\lambda)$ and $\phi_i(\lambda)$ of the species are known and the spectral range is fully covered by the measurements. Spectroradiometers are usually equipped either with one monochromator and a diode array detector or with double monochromators and a photomultiplier. The former is fast but might be susceptible to stray light. The latter is slow owing to the wavelength scanning but precise (Shetter and Müller, 1999; Hofzumahaus et al., 1999). The last technique is the filter radiometry. In this technique, a photo detector measures the intensity of the solar actinic flux through optical filters, which are carefully selected so that the spectral response of the instrument resembles the wavelength dependence of the product of the absorption cross section and the dissociation quantum yield of the pertinent molecule (Junkermann, 1994; Volz-Thomas et al., 1996). In spite of the simple detection scheme, only one J value can be measured by one instrument because the selection of the optics is specific. To date, filter radiometers for $J(NO_2)$ and $J(O^1D)$, the photolysis frequency of O_3 to give an $O(^1D)$ atom, have been developed and are commercially available. They are widely used during recent field campaigns to investigate photochemistry (Carpenter et al., 1997; Früh et al., 2000; Kanaya et al., 2001).

Photolysis frequencies can also be calculated by a theoretical approach, where actinic fluxes are calculated with a radiative transfer model. The conversion of actinic fluxes to J values can be made in the similar manner to the spectroradiometry. Although a radiation field with clouds is difficult to simulate, those under cloudless conditions are well simulated by including scattering and absorption by aerosols and gaseous components into the model.

J values obtained using these experimental techniques have been compared with each other or with those from the theoretical approach during field studies (Kelley et al., 1995; Müller et al., 1995; Lantz et al., 1996; Shetter et al., 1996; Kraus et al., 2000; Früh et al., 2000). Recently, the most comprehensive field campaign called International Photolysis Frequency Measurement and Modelling Intercomparison campaign (IPMMI) was performed in Colorado in 1998, in which a blind intercomparison was made among 16 radiative transfer models, three spectroradiometers, and some other instruments (McKenzie et al., 2002, and references therein). Actinic fluxes measured by a spectroradiometer over Greece have also been compared with those from an elaborate model including observed aerosol properties (Hofzumahaus et al., 2002). These studies provided us with better knowledge of the radiative transfer especially in the 280–420 nm region. However, these comparisons did not necessarily result in perfect agreement, suggesting that there are still problems either with observation techniques, absorption cross section data employed to calculate J values, or theoretical calculations.

We have deployed a $J(NO_2)$ filter radiometer and a spectroradiometer equipped with a single monochromator and a diode array detector during RISOTTO 2000 intensive field campaign performed in Rishiri Island, in June 2000. By comparing the actinic fluxes (295–700 nm) under clear conditions determined by the spectroradiometer and by the TUV radiative transfer model, we first checked the performance of the spectroradiometer. After that, J values of more than 20 chemical species were calculated from the observed actinic flux. The $J(NO_2)$ values from the spectroradiometer and the filter radiometer were compared under both clear and cloudy conditions. Additionally, transmission factors due to clouds and aerosols were calculated as a function of wavelength and were studied in detail.

2. Experimental

The spectroradiometer used in this work was manufactured by Meteorologie Consult GmbH in Germany. The downwelling solar light is first received by a smoked quartz dome, which is carefully designed for isotropic light collection. An artificial horizon made of anodized aluminum prohibits the detection of upwelling sunlight. After being collected by the dome, the solar light is guided to the entrance of a monochromator (Carl Zeiss) by a quartz rod and a round-to-slit converter. The monochromator has a fixed grating (248 lines mm^{-1}) and resolves the sunlight spectrally between 280 and 700 nm, whose intensities are then measured by a diode array detector with 512 pixels (Hamamatsu Photonics). The stray light rejection ratio of the monochromator is $>10^3$. All of these components are located in a shielded aluminum housing directly attached to the quartz dome. The signal for each pixel is averaged for four integration time periods (0.5, 1, 2, and 5 s) and transferred to a personal computer through a 15-bit analog-to-digital converter. In the computer, each spectrum for the four integration periods is averaged every minute and then stored. The wavelength is calibrated with Hg lines from

a low-pressure mercury lamp to within 0.3 nm. These line source measurements also suggest that the wavelength resolution was around 1.8 nm. The wavelength drift is small (5×10^{-4} nm K^{-1}) and the spectral reproducibility is better than 0.01 nm.

The background signal is composed of two main parts, the thermal background signal and the stray light signal. The thermal one can be observed as a diurnal change in the baseline level while the quartz dome is completely capped. This component is confirmed to be constant throughout the wavelength range. The second term is noticed as a signal increase in the 285–295 nm region due to solar light, where solar photons must be efficiently absorbed by ozone present in the upper atmosphere and no signal is expected. It is assumed that the stray light signal is also constant for all the pixels. The total background level is determined by the signal level averaged over the 285–295 nm region and is subtracted from the raw signal for all the pixels before analysis. However, the stray light problem is not fully avoided in the UV-B region even with this treatment as detailed later. The signal after background subtraction is converted into an absolute value of actinic flux in quanta cm^{-2} s^{-1} nm^{-1} by applying wavelength-dependent calibration factors. We performed calibrations of the spectroradiometer using a standard quartz halogen lamp (500 W, Ushio Inc.) whose spectral irradiance at 50 cm has been specified. Since the photon fluxes for the 300–400 nm region were weak at that distance, calibrations were also made with the lamp placed at 15 and 25 cm to the radiometer to obtain calibration factors with less uncertainty. For such calibrations with shorter distances, absolute fluxes were estimated by multiplying the ratio of the measured signal at the short distance to that at 50 cm in the visible region by the specified irradiance. The random uncertainty (1σ) of calibration factors was estimated to be $\pm4\%$ for 300 nm and $\pm2\%$ for >320 nm from reproducibility. Considering the uncertainty (1σ) in the specified absolute flux of the standard lamp of $\pm2.6\%$ for 250–360 nm and $\pm1.6\%$ for 360–830 nm, we estimated that the total uncertainty (1σ) in the calibration factor was $\pm5\%$ for 300–320 nm, $\pm4\%$ for 320–360 nm, and $\pm3\%$ for 360–700 nm.

From the calibrated actinic flux spectra with four integration time periods, an optimal spectrum is extracted every minute so that the data with the highest signal level and without saturation are employed for each wavelength. Usually in the daytime, long integration resulted in saturation with the visible wavelength region where the actinic flux and the sensitivity are both high. Typically, an optimal spectrum is composed of the actinic fluxes for <340 nm determined with the 5-s integration, 340–400 nm with the 2-s integration, 400–430 nm with the 1-s integration, and >430 nm with the 0.5-s integration during midday. The vertical resolution of the digitally measured actinic fluxes was 6.0×10^{9}, 1.1×10^{10}, 1.3×10^{10}, and 2.7×10^{10} quanta cm^{-2} s^{-1} nm^{-1} at 320 nm (5-s integration), 370 nm (2-s integration), 420 nm (1-s integration), and 550 nm (0.5-s integration), respectively.

The $J(NO_2)$ filter radiometer used in this work was also manufactured by Meteorologie Consult (Volz-Thomas et al., 1996). The instrument has two 2-π sr collecting optics enabling simultaneous measurements of upwelling and downwelling components of $J(NO_2)$. In this study, only the downwelling component is used for comparison with $J(NO_2)$ derived from the spectroradiometer. The filter radiometer was calibrated by the manufacturer with $\pm5\%$ accuracy. The two radiometers were installed at the observatory located at 45.07°N, 141.12°E, and 30 m above sea level (Tanimoto et al., 2000), in the southern part of Rishiri Island, Japan. They were fixed at a high position of 6 m above ground level to have a horizontal view of 360°.

The radiative transfer model TUV ver. 4.1a (Madronich and Flocke, 1998) was utilized to calculate actinic fluxes under clear-sky conditions. The calculations were made with the radiative transfer scheme of the pseudo-spherical 8 stream discrete ordinates. The wavelength resolution was 1 nm. The total column ozone amount was set to 332 Dobson units as measured by the TOMS-EP satellite sensor on 25 June 2000, and was distributed vertically as the profile of US Standard Atmosphere of 1976. The background aerosol optical thickness was assumed to be 0.38 at 340 nm, and its vertical profile was taken from Elterman (1968). The albedo was assumed to be 0.1 independently of wavelength to reproduce the ratio of upwelling to downwelling $J(NO_2)$ measured by the filter radiometer.

3. Actinic flux comparisons

Fig. 1 shows the spectral actinic fluxes observed by the spectroradiometer and calculated with the TUV model at noon of 25 June 2000, under cloudless conditions. The solar zenith angle (SZA) was 22.1°. Since the wavelength resolution for the measurements is coarser than that for the calculation, the Fraunhofer lines appear more sharply for the calculated spectrum. The difference at 688 nm is due to the B band of O_2, not included in the TUV calculation. The TUV model slightly overpredicts actinic fluxes for >550 nm, partly due to the water vapor absorption not considered in the model. Except them, the two quantities basically agree very well with each other, attesting the good performance of the spectroradiometer. However, in the inset graph where the 295–320 nm region is magnified, the measured actinic flux for <302 nm is significantly higher than that modeled. The difference cannot be attributed to the difference of the wavelength resolution or to the uncertainty in the ozone absorption cross section.

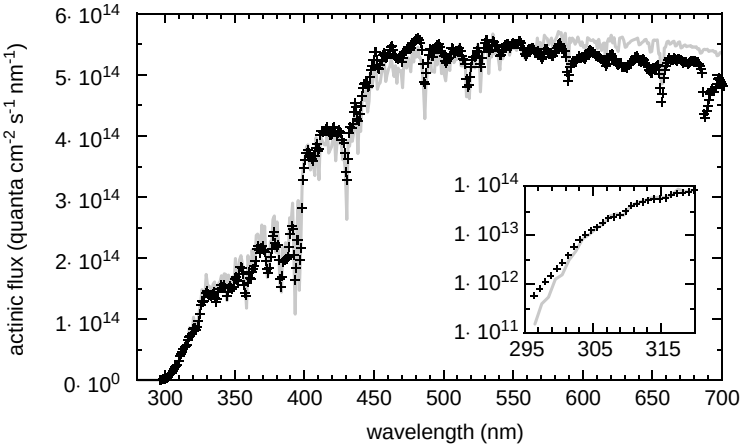

Fig. 1. Actinic fluxes from the spectroradiometer (plus marks) and from the TUV radiative transfer model (gray line) for 1200 local standard time (LST) on 25 June 2000. The SZA is 22.1°. The 295–320 nm region is magnified in the inset graph.

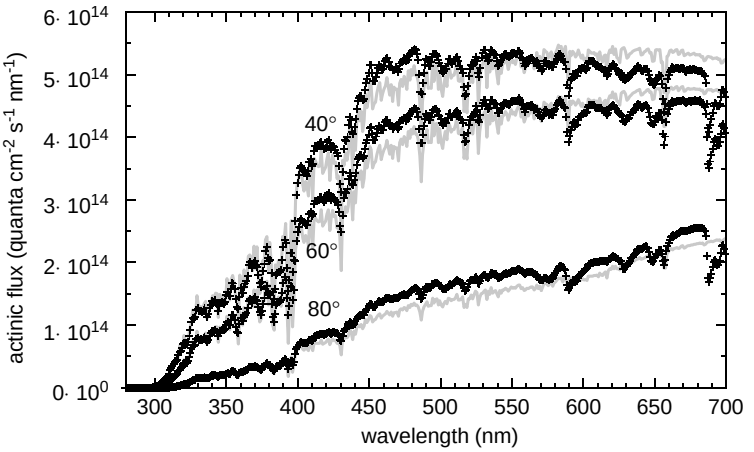

Fig. 2. Same as Fig. 1 but for larger SZAs. From top to bottom, 40° (0852 LST), 60° (0657 LST), and 80° (0459 LST on 25 June 2000).

A spectroradiometer equipped with one monochromator similarly designed by Meteorologie Consult has resulted in a still higher actinic flux in the UV-B region during the IPMMI field campaign. The cause for this high value might be wavelength-dependent stray light presumably caused by the reflection between the diode array detector and its glass cover (R. Schmitt, personal communication, 2001). The stray light level as determined by the signal level for 285–295 nm corresponds to $<1.7\times10^{12}$ and $<1.1\times10^{12}$ quanta $cm^{-2}\,nm^{-1}\,s^{-1}$ for 300 and 400 nm, respectively. Considering the absolute values of the solar actinic flux, even only slight dependence of the stray light upon wavelength can be a problem at 300 nm, while it is negligible for longer wavelengths. This problem makes the $J(O^1D)$ values derived from the spectroradiometer that are sensitive to the UV-B flux positively biased as discussed later.

Measured and calculated actinic fluxes at larger SZAs (40°, 60°, and 80°) on the same day are also compared in Fig. 2. Except for the stray light problem in the UV-B region, the two fluxes agree quite well to each other. The difference for the conditions of SZA $\leqslant 60°$ and wavelength >320 nm was within 10%, although the measured actinic fluxes tended to be higher by up to 20% at large SZAs for >400 nm. For SZA $>75°$, the collection optics may show a decline in sensitivity toward direct solar radiation (Volz-Thomas et al., 1996; Hofzumahaus et al., 1999), and this does not explain the observed higher values. Rather, this tendency might be due to the albedo increase associated by large SZAs (Payne, 1972) or due to the non-perfect treatment of the spherical atmosphere in the model. These comparisons suggest that our spectroradiometer is suitable for measurements in the 320–700 nm region,

although a rigorous quantitative test requires the intercomparison against another absolute instrument because the radiative transfer model calculations contain uncertain assumptions on aerosol properties, vertical profiles of ozone and aerosols, and albedo.

4. J value calculations and comparisons

4.1. $J(NO_2)$ calculations and comparisons

By convoluting the 1-min actinic fluxes by the spectroradiometer with the absorption cross section of NO_2 (Harder et al., 1997) and its quantum yield (DeMore et al., 1997), downwelling $J(NO_2)$ values were calculated. The uncertainty in the calculated $J(NO_2)$ is estimated to be $\pm 12\%$ (1σ), from the uncertainty of the actinic flux calibration ($\pm 4\%$), the effects of a wavelength shift by 0.3 nm ($\pm 1\%$) and the wavelength resolution of 1.8 nm ($\pm 1\%$), and the uncertainties of the absorption cross section ($\pm 4\%$) and the quantum yield ($\pm 10\%$). They are then compared with the 2-π component of the $J(NO_2)$ observed with the filter radiometer. Fig. 3 shows the comparison for 3 days, where nearly perfect agreement is ascertained even on cloudy days. Fig. 4 shows the composite diurnal variation of the ratio of $J(NO_2)$ from the spectroradiometer to that from the filter radiometer produced from the data over 20 days (7–26 June 2000). The ratio is almost unity whenever SZA is $<85^\circ$ and $J(NO_2)$ is greater than $10^{-4}\,s^{-1}$. The slope of the regression line for the scatterplot between the two values (not shown) was 0.982, with the value from the filter radiometer being only 1.8% higher. In Fig. 5, it is illustrated that clear-day $J(NO_2)$ values from the spectroradiometer, filter radiometer, and the TUV model plotted against SZA are quite well compared to each other. Therefore, we conclude that the determination of 2-π $J(NO_2)$ during the field campaign is no worse than 10%. At Rishiri Island, observed NO/NO_2 ratios were around 0.2 even during midday, quite lower than the values expected with conventional chemistry that includes NO_2 photolysis and NO oxidation by O_3 and peroxy radicals (Kanaya et al., 2002):

$$\text{Ratio} = \frac{J(NO_2)}{k[O_3] + k'[HO_2] + \sum k_i''[RO_2]}. \quad (2)$$

The good determination of $J(NO_2)$ was critical for reducing the uncertainty of this calculated ratio and enabled us to conclude that the difference from the observed NO/NO_2 ratio is statistically significant and to hypothesize the importance of iodine chemistry (Kanaya et al., 2002).

In Fig. 5, the SZA dependence of $J(NO_2)$ is also compared with values obtained during other studies made at near sea level under clear conditions. Our values

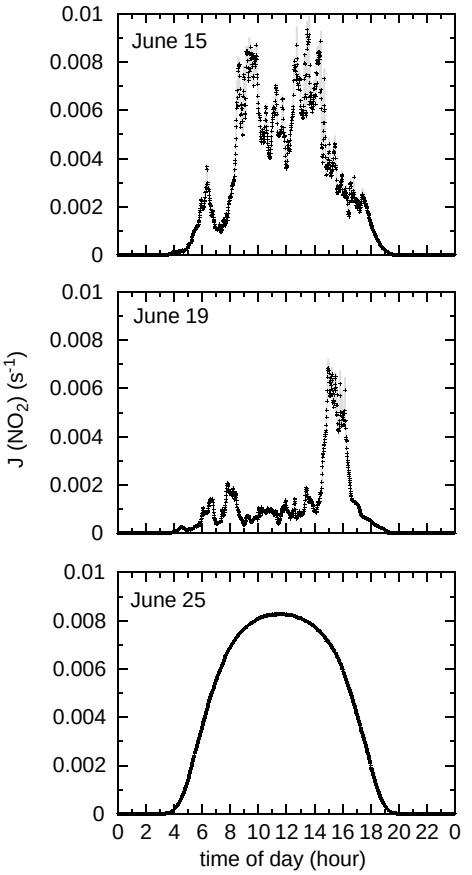

Fig. 3. Comparison between 2-π $J(NO_2)$ values measured by the spectroradiometer (plus marks) and by the filter radiometer (gray line) for selected 3 days, 15, 19, and 25 June 2000.

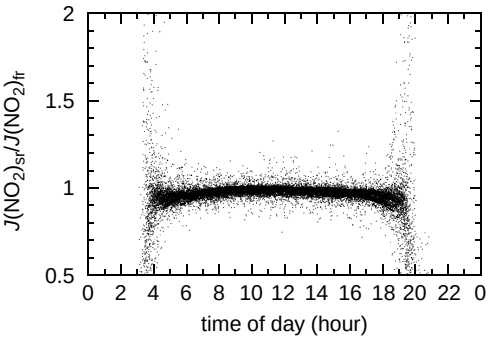

Fig. 4. Composite diurnal variations of the ratio of $J(NO_2)$ from the spectroradiometer to that from the filter radiometer. Data over 20 days (7–26 June 2000) are included.

are higher than the recent precise determination of the 2-π $J(NO_2)$ using a spectroradiometer with double monochromators in Germany (Kraus and Hofzumahaus, 1998) by around 10%. It is likely that the difference came from the lower absorption cross sections

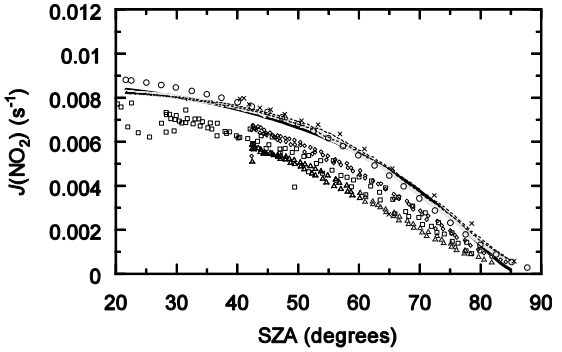

Fig. 5. 2-π $J(NO_2)$ values from the spectroradiometer (gray line) and the optimized fitting curve (solid line) on 25 June under cloudless condition. 2-π $J(NO_2)$ values from the filter radiometer (broken line) and the TUV model (open circles) are included for comparison. Our values are also compared with the values from other studies: data derived from a spectroradiometer (Kraus and Hofzumahaus, 1998), open diamonds; those from a filter radiometer in Germany (Kraus and Hofzumahaus, 1998), open triangles; those from a filter radiometer over the Atlantic Ocean (Brauers and Hofzumahaus, 1992), open squares; those from a radiometer based on pressure change due to NO_2 photolysis (Madronich et al., 1983), crosses.

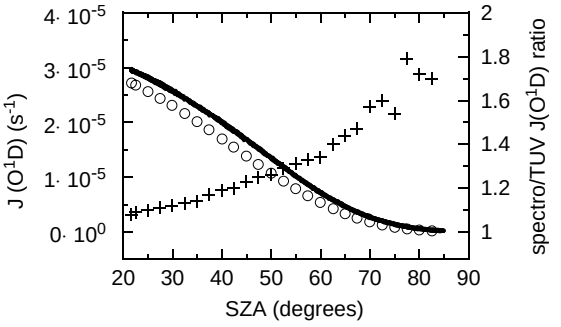

Fig. 6. $J(O^1D)$ values from the spectroradiometer (solid dots) and from the TUV actinic flux (open circles) as functions of SZA on a cloudless day. The ratio of the two $J(O^1D)$ values as a function of SZA (plus marks, right axis).

in the 350–380 nm range they employed (Harwood and Jones, 1994), not from the differences in the measured actinic fluxes. The values from their filter radiometer are much lower than ours, and the reason remains unknown. The filter radiometer values obtained by Brauers and Hofzumahaus (1992) over the Atlantic are between the two series from Kraus and Hofzumahaus (1998), although the difference from our values is small for SZA $<40^\circ$. The values observed in Canada (Madronich et al., 1983) show close agreement with our values. From the limited data available, our $J(NO_2)$ values seem to be reasonable.

4.2. $J(O^1D)$ from spectroradiometer

As mentioned earlier, the spectroradiometer suffered from a stray light problem in the UV-B region, resulting in overestimation of $J(O^1D)$. Fig. 6 shows the $J(O^1D)$ values from the spectroradiometer and the radiative transfer model in the morning of 25 June under clear conditions as functions of SZA. The absorption cross section and the quantum yield were taken from Daumont et al. (1992) and Sander et al. (2000), respectively. The ratio of the measured to calculated $J(O^1D)$ can be read with the right axis, indicating that the degree of the overprediction was $<20\%$ for SZA $< 40^\circ$ and 35% for SZA $= 60^\circ$. Actually, this disagreement in $J(O^1D)$, which defines its uncertainty range, is larger than that of $J(NO_2)$ and propagates errors to radical mixing ratios estimated within a photochemical box model. However, Monte Carlo calculations with our photochemical box model suggested that the uncertainties in $J(O^1D)$ of factors of 1.2 and 1.4 at 1200 and 1600 local standard time (LST) brought the uncertainties of only 11% and 15% in OH concentrations and 6.5% and 9.5% in HO_2 concentrations, respectively. Considering that the uncertainties in calculated radical concentrations stemming from all the uncertainties including those of rate constants of important chemical reactions, photolysis frequencies, and precursor concentrations are typically $\pm 28\%$ for OH and $\pm 19\%$ for HO_2 at Rishiri Island (Kanaya et al., 2002), these uncertainties solely from the $J(O^1D)$ uncertainties are not very large to govern the full uncertainty. Additionally, they are smaller than the uncertainties in observed HO_x concentrations ($\pm 24\%$ and $\pm 26\%$ for OH and HO_2). Therefore, this stray light problem is not fatal for the comparisons of radical mixing ratios at this stage, although elimination of the stray light problem is straightforward to make more precise comparisons.

4.3. J values of other atmospheric species

J values of CH_2O, H_2O_2, CH_3OOH, and HONO, which are all important to radical production, were also determined. Since all of these species dissociate upon photon absorption with the wavelength of 290–420 nm, spectral actinic flux measurements reported to date usually cover this wavelength range only (e.g. Shetter and Müller, 1999; Hofzumahaus et al., 1999). Recently, however, the importance of halogen chemistry in the troposphere has been increasingly recognized (e.g. Platt, 2000). Some halogenated compounds, for example, halogen molecules such as Br_2 and I_2 and hypohalogenous acids such as HOBr and HOI, show significant absorption in the >420 nm region. The spectroradiometer used here has an advantage of broadband coverage up to 700 nm and enables us to determine their J values to study halogen chemistry in detail. Table 1

Table 1
Calculated J values and three parameters for approximation for clear-sky conditions

Photolysis	Products	L	M	N	Absorption cross section	Quantum yield	Total uncertainty (%)
NO_2	$NO + O(^3P)$	1.200E−02	0.2139	0.3193	Harder et al. (1997)	DeMore et al. (1997)	±12
HONO	OH + NO	2.110E−03	0.2608	0.3276	Bongartz et al. (1994)	Unity	±16
HCHO[a]	H + CHO	3.930E−05	0.7492	0.3733	Cantrell et al. (1990)	DeMore et al. (1997)	±12
HCHO	$H_2 + CO$	5.880E−05	0.5094	0.3356	Cantrell et al. (1990)	DeMore et al. (1997)	±14
CH_3OOH[a]	$CH_3O + OH$	6.570E−06	0.7167	0.2938	Vaghjiani and Ravishankara (1989)		±50
H_2O_2[a]	2OH	8.520E−06	0.7200	0.3385	DeMore et al. (1997), 285 K		±26
N_2O_5[a]	$NO_3 + NO_2$	5.260E−05	0.6950	0.3084	DeMore et al. (1997), 285 K		
NO_3	$NO + O_2$	2.400E−02	0.0289	0.1854	Graham and Johnston (1978), DeMore et al. (1997) for >600 nm	TUV source code	±50
NO_3	$NO_2 + O(^3P)$	2.020E−01	0.0095	0.2106	Graham and Johnston (1978), DeMore et al. (1997) for >600 nm	TUV source code	±50
PAN[a]	Products	8.730E−07	1.2490	0.1316	Talukdar et al. (1995)		
Cl_2	2Cl	2.960E−03	0.3702	0.3063	DeMore et al. (1997), 285 K		±21
Br_2	2Br	4.370E−02	0.0369	0.2606	Passchier et al. (1967)		±20
I_2	2I	1.912E−01	0.0019	0.2185	Tellinghuisen (1973)		
BrCl	Br + Cl	1.400E−02	0.1152	0.2829	Maric et al. (1994)		±20
ICl	I + Cl	3.042E−02	0.0224	0.2558	Seery and Britton (1964)		
IBr	I + Br	8.909E−02	0.0050	0.2400	Seery and Britton (1964)		
HOCl	OH + Cl	3.470E−04	0.4817	0.3038	Sander et al. (2000)		
HOBr	OH + Br	2.800E−03	0.2592	0.2712	DeMore et al. (1997)		
HOI	OH + I	1.037E−02	0.1766	0.3010	Rowley et al. (1999)		
BrO	$Br + O(^3P)$	4.820E−02	0.3960	0.3337	Wahner et al. (1988)		±51
IO	$I + O(^3P)$	3.079E−01	0.0622	0.3021	Harwood et al. (1997)		
$ClONO_2$[a]	$Cl + NO_3$	4.840E−05	0.4549	0.2837	DeMore et al. (1997), 285 K	DeMore et al. (1997)	±31
$ClONO_2$	$ClO + NO_2$	1.180E−05	0.5689	0.4858	DeMore et al. (1997), 285 K	DeMore et al. (1997)	±31
$BrONO_2$	Products	1.760E−03	0.3029	0.2751	Burkholder et al. (1995)		±41
CH_3I[a]	$CH_3 + I$	9.100E−06	0.7362	0.4904	Roehl et al. (1997), 285 K		±21
CH_2ICl[a]	Products	1.948E−04	0.8508	0.3213	Roehl et al. (1997), 285 K		±21
CH_2IBr[a]	Products	6.609E−04	0.7754	0.3226	Mössinger et al. (1998), 285 K		
CH_2I_2	Products	1.095E−02	0.6258	0.3323	Mössinger et al. (1998), 285 K		±21

Based on 2-π sr spectroradiometric measurements on 25 June 2000 at Rishiri Island with total ozone (TOMS-EP) = 332 DU.
[a] J values contributed from wavelength of <320 nm by more than 30%.

lists the J values determined in this work with the references from which absorption cross sections and quantum yields were taken. The J values contributed from the <305 nm wavelength region by more than 10% including $J(O^1D)$ are excluded from the table, which are likely to suffer from the stray light problem. The absorption cross sections and the quantum yields at room temperature are used unless otherwise noted. The total uncertainties for several J values are estimated in the similar way to the calculation of the $J(NO_2)$ uncertainty, except that the uncertainties of absorption cross sections are determined from the degree of agreement among three or more reliable studies, which dominate the total uncertainties. No values are shown if less numbers of studies are available.

5. J value parameterization

Here we propose parameterizing the J values of more than 20 species as functions of SZA, so that they are easily included in a photochemical box model. First, those under clear conditions are approximated using three parameters for each. For cloudy conditions, it is tested whether the transmission factor, defined as the ratio of an actinic flux at a certain wavelength to that under clear conditions at the same SZA, is constant over the 320–700 nm region. If this is true, any J values under cloudy conditions can be calculated only by multiplying the single transmission factor to those under clear conditions.

5.1. Clear-sky conditions

The clear-sky J values obtained during the morning on 25 June were approximated with three parameters, L_i, M_i, and N_i, by the following equation as suggested by Hough (1988) and Jenkin et al. (1997):

$$J_i(\mathrm{SZA}) = L_i \cos(\mathrm{SZA})^{M_i} \exp(-N_i \sec(\mathrm{SZA})). \quad (3)$$

Fig. 5 includes the example of the fitting for the 2-π component of $J(NO_2)$. It is demonstrated that the observed SZA dependence is quite well reproduced by the three parameters. The three parameters determined for all the J values are listed in Table 1. The J values contributed from the <320 nm region by more than 30% are marked with "a" letters. They can be influenced by the column ozone amount, and the listed parameters for them might not be valid when the column ozone amount is exceptionally low or high. Even for the other J values without "a" letters, different amounts of aerosols or different surface albedo may obscure general application of the results to other locations. Nonetheless, sensitivity calculations using the TUV model showed that the changes in the albedo and in the aerosol optical depth by $\pm 50\%$ resulted in only $<7\%$ shifts in the 2-π actinic flux for 320–700 nm when SZA $< 60^\circ$. The shifts are still smaller than the total uncertainties of J values mainly contributed from the uncertainty of absorption cross sections. Thus, the parameters for these J values may also be useful at different places as long as the conditions of albedo and aerosol loading are satisfied, assisting photochemical modeling studies at sea level.

5.2. Cloudy conditions: transmission factors at various wavelengths

The actinic flux observed with a time resolution of 1 min was divided by that of the morning on 25 June with the same SZA under cloudless condition, to give transmission factors (TF) for each wavelength. Here we examine thus calculated TFs for the >320 nm wavelength region, where the influence from day-to-day variations in the total column ozone amount and from the stray light problem would be negligible. Figs. 7a–c are the scatterplots between TFs at 323.2, 399.1, and 666.2 nm and that at 409.9 nm for SZA $<60^\circ$. The relationship is the most compact for Fig. 7b, where the

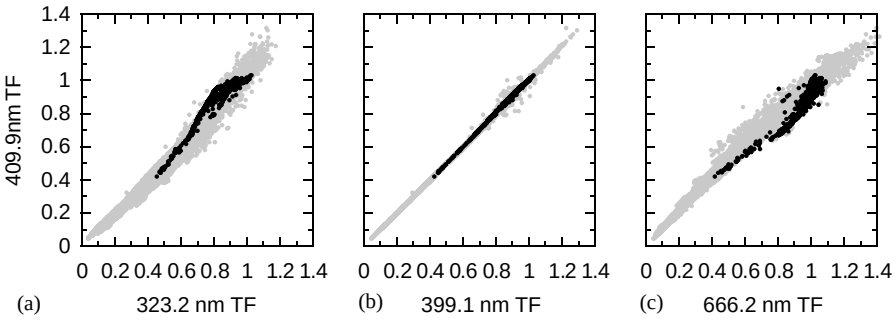

Fig. 7. Scatterplots between TFs at (a) 323.2 nm, (b) 399.1 nm, and (c) 666.2 nm and that at 409.9 nm for SZA $<60^\circ$. Data over 20 days are shown by gray points. Data on 22–24 June are shown by black points.

TFs at the nearest wavelengths are compared. The tenth and 90th percentiles for the ratio of TF(323.2 nm) to TF(409.9 nm) are 0.91 and 1.14, while those for the ratio of TF(666.2 nm) to TF(409.9 nm) are 0.90 and 1.08, suggesting that the TFs for the 320–700 nm region are usually within 15% of those at 409.9 nm. This analysis allows us to calculate J values under cloudy conditions within 15% by scaling the J values under clear conditions for the pertinent SZA using a TF at a single wavelength. Even without spectroradiometric measurements, the TF for $J(NO_2)$ can easily be determined by dividing the $J(NO_2)$ observed with a filter radiometer by that under clear conditions, which can be used as scaling factors for other J values.

However, slight curvatures are present in Figs. 7a and c, suggesting that the TF is higher for the shorter wavelength when it is less than unity. Fig. 8 shows the dependence of TF on wavelength at local noon (SZA = 21.7°), at 0850 and 1422 LST (SZA = 40°), and at 0655 and 1616 LST (SZA = 60°) on 14 June, a cloudy day. The structures found in the >570 nm region are mostly due to the different absorbance of water vapor, and are not discussed here. Although TF is fairly constant at noon and 1424 LST throughout 320–700 nm, it decreases with wavelength at different timings, especially with large SZAs. A similar tendency has been recorded for the irradiance of the 300–420 nm region (Seckmeyer et al., 1996), or noted as the difference of TFs for $J(NO_2)$ and $J(O^1D)$ (Crawford et al., 1999). Frederick and Erlick (1997) found the same trend for an extended wavelength region (300–600 nm). This behavior can arise from Rayleigh backscattering of sunlight beneath the cloud, followed by reflection of this upwelling radiation from the cloud base back to the ground (Frederick and Erlick, 1997). The presence of clouds that block only the direct radiation and do not affect the scattered fraction may also result in this tendency, since the scattered fraction dominates the total flux in the short wavelength region. Unfortunately, we did not perform cloud monitoring during the field campaign and could not characterize the transmission with respect to cloud types and locations in detail here.

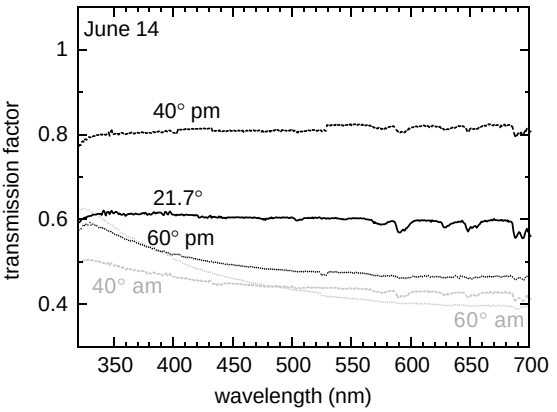

Fig. 8. TFs as functions of wavelength at five selected timings on 14 June, when clouds mainly attenuated the fluxes. Local noon (SZA = 21.7°), at 0850 and 1422 LST (SZA = 40°), and at 0655 and 1616 LST (SZA = 60°).

The data points from 3 days, 22–24 June, shown by black circles in Fig. 7, are the exceptions from the tendency. Fig. 9 shows the temporal variations of the TFs at 6 wavelengths for SZA <60°. TF increases with wavelength for 3 days, while it does not on the other days even with rapid changes. The sky was almost cloudless on these days except for the morning of 24 June. This episode is studied in detail in the next section.

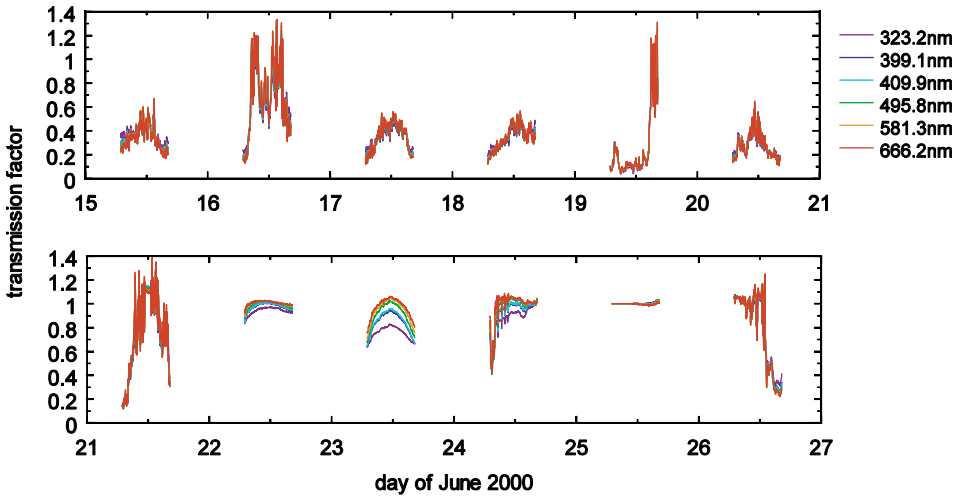

Fig. 9. Temporal variations in TFs at 6 wavelengths (323.2, 399.1, 409.9, 495.8, 581.3 and 666.2 nm) for SZA <60° over 12 days.

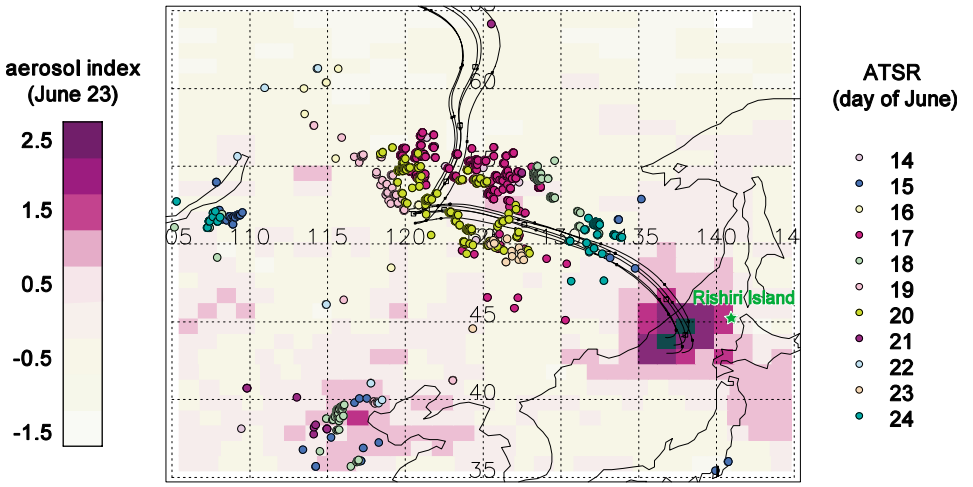

Fig. 10. Aerosol index as measured by the TOMS-EP sensor on 23 June 2000 (colored contour), isentropic backward trajectories from the central area of the aerosol plume with the end time of 0900 LST on 23 June and with the end altitude of 3000 m (solid lines), and the hot spots detected by the ATSR satellite sensor during 14–24 June 2000 (colored circles).

6. Detection of an aerosol plume from the forest fire

It is widely recognized that aerosols are important to radiative transfer as well as clouds. Studies incorporating aerosols into radiative transfer models have suggested that the solar actinic flux or irradiance at the Earth's surface can be depleted (Liao et al., 1999; Erlick and Frederick, 1998) or even enhanced (Jacobson, 1998) under cloudless conditions. Since the Mie scattering and absorption coefficients of tropospheric aerosols are usually higher with shorter wavelength, the actinic flux at surface should be weakened more strongly at shorter wavelength. This tendency is opposite from that induced by clouds. Accordingly, the trend observed on 22–24 June is easily explained by aerosols, if present.

Actually, the TOMS-EP satellite sensor detected aerosols over the northern part of the Japan Sea during this period. Fig. 10 shows the geographical distribution of the TOMS aerosol index (AI) on 23 June. The AI is a measure of the change of spectral contrast in the near UV due to radiative transfer effects of aerosols in a Rayleigh scattering atmosphere (Torres et al., 2002). The positive value over the area suggests the presence of absorbing aerosols. This figure includes the hot spots detected by the ATSR satellite sensor (Arino et al., 1999) during 14–24 June, which usually correspond to the locations of forest fire and biomass burning. It is clearly shown that there were intense forest fires near the borderline between Russia and China during this period. Although not shown, the AVHRR satellite sensor also detected fires and smokes in this region. Fig. 10 also includes the isentropic backward trajectories from the center of the plume (43.5°N, 137.075°E) and four locations displaced from the center by 0.5° for both

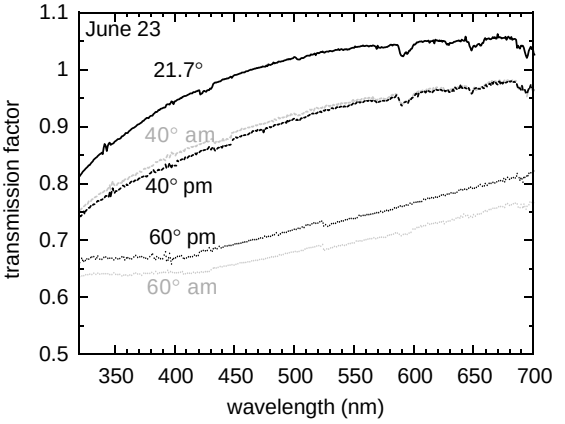

Fig. 11. TFs as functions of wavelength at five selected timings on 23 June, when aerosols mainly attenuated the fluxes. Local noon (SZA = 21.7°), at 0851 and 1424 LST (SZA = 40°), and at 0657 and 1618 LST (SZA = 60°).

latitude and longitude. The trajectories were calculated with the end time of 0900 LST (0000 UT) of 23 June and the end altitude of 3000 m using the ECMWF reanalysis data as a meteorological field. They have passed over the region with intense forest fires detected on 20 June at an altitude of 1900 m, and it is likely that aerosols were put into the air mass there. The trajectories with the end altitude lowered to 1000 and 2000 m came from the northern region and did not pass over the fires. Thus, it is likely that the plume with aerosols was present at a high altitude around 3000 m and the surface air mass was less influenced. At the observatory, neither the measurements of CO, number density of aerosols with

Table 2
Transmission factors of J values on 23 June with respect to 25 June due to aerosol plume

Local time	SZA (degree)	TF of $J(O^1D)$	TF of $J(NO_2)$	TF of $J(NO_3 \rightarrow NO_2 + O^3P)$
0657	60	0.60	0.64	0.70
0851	40	0.72	0.82	0.94
1127–1134, 1141–1148	21.7	0.76	0.90	1.03
1424	40	0.70	0.81	0.94
1618	60	0.62	0.67	0.74

0.1-5 μm size, nor the chemical composition of filtered aerosols showed any signatures of forest fires. This is consistent with the backward trajectory analysis. This situation is different from the case where elevated CO concentrations were detected at the observatory in August–October, 1998 (Tanimoto et al., 2000). The flowing altitude of the plume may depend on conditions. Column CO enhancements were detected by ground-based FTIR measurements at Moshiri and Rikubetsu, 125 and 275 km southeast of Rishiri Island, in June 2000 (L. Yurganov, personal communications, 2002), suggesting that the influence of forest fires was only sensed by column measurements this time.

At any rate, it is likely that the aerosols are responsible to the wavelength dependence of TF during 3 days. Fig. 11 shows the wavelength dependence of TF for SZA = 21.7°, 40°, and 60° on 23 June. The trend is clearly opposite to that induced by clouds shown in Fig. 8. The increase in TF with wavelength is more significant in 320–500 nm rather than in 500–700 nm when SZA $<40°$. TF is even higher than unity for >465 nm at noon, suggesting that the aerosol layer enhanced the actinic flux when compared to clear-sky conditions in this wavelength region. At SZA = 60°, the increase in TF takes place in a longer wavelength region. The tendency was similar for morning and afternoon with the same SZA, suggesting that the aerosol layer with a single optical property was persistently present over the day.

Finally, the transmission of J values on 23 June with this aerosol episode is summarized in Table 2. TF is small at large SZAs and for J values sensitive to fluxes at short wavelengths. The second channel of $J(NO_3)$ that yields NO_2 and $O(^3P)$ was even enhanced at local noon by 3%, due to the enhancement of the actinic flux in the 500–650 nm region. The TFs for $J(O^1D)$ are listed here, although the results may be influenced by the day-to-day fluctuations of the wavelength-dependent stray light. $J(O^1D)$ is lower by 24% at noon or by 40% at SZA = 60°. The total ozone column density on 23 June was 338 DU, higher than that on 25 June, 332 DU. However, the slight difference cannot fully explain the low $J(O^1D)$ on 23 June, suggesting the potential influence of the aerosols. From long-term data of the TOMS-EP aerosol index, even higher values can be easily found elsewhere if covered with plumes from biomass burning, forest fires, or dust storms. It is necessary to include shifts in J values due to aerosols in order to simulate photochemistry below the aerosol layers appropriately.

7. Summary

Actinic fluxes measured by a spectroradiometer equipped with a single monochromator/diode array detector at Rishiri Island in June 2000 agreed well with those calculated with the TUV radiative transfer model for SZA $<80°$ throughout the UV-A to visible wavelength region. Although the actinic flux from the spectroradiometer resulted in a higher value in the UV-B region due to insufficient stray light rejection, the overestimation introduced only $<15\%$ overprediction to daytime OH and HO_2 radical concentrations when calculated in a photochemical box model. The $J(NO_2)$ values from the spectroradiometer agreed quite well with those from a filter radiometer on both clear and cloudy days. J values of various chemical species in the atmosphere were computed with the actinic flux from the spectroradiometer. Each J value under clear conditions was approximated as a function of SZA using three parameters. As a first approximation, the transmission by clouds was found to be nearly constant throughout 320–700 nm, suggesting that a single TF could be used as a linear scaling factor to calculate any J values under cloudy conditions within 15%. TF showed a slight decrease with wavelength in the presence of clouds, consistent with past studies. During 22–24 June, an aerosol plume probably originating from forest fires in Russia covered the island, and the reduction of the actinic flux is stronger at shorter wavelengths. This suggests the need of spectroradiometric measurements of actinic fluxes to determine J values if high amounts of aerosols are present.

Acknowledgements

The authors are grateful for all the participants of the campaign RISOTTO 2000 summer intensive. Shamil

Maksyutov and Pakpong Pochanart are thanked for help in the backward trajectory calculations. This work is financially supported by CREST (Core Research for Evolutional Science and Technology) of the Japan Science and Technology Corporation.

References

Arino, O., Rosaz, J-M., Melinotte, J-M., 1999. World Fire Atlas with AVHRR and ATSR, Proceedings of the IUFRO Conference on Remote Sensing and Forest Monitoring, Rogow, Poland.

Bongartz, A., Kames, J., Schurath, U., 1994. Experimental determination of HONO mass accommodation coefficients using two different techniques. Journal of Atmospheric Chemistry 18, 149–169.

Brauers, T., Hofzumahaus, A., 1992. Latitudinal variation of measured NO_2 photolysis frequencies over the Atlantic Ocean between 50°N and 30°S. Journal of Atmospheric Chemistry 15, 269–282.

Burkholder, J.B., Ravishankara, A.R., Solomon, S., 1995. UV/visible and IR absorption cross sections of $BrONO_2$. Journal of Geophysical Research 100, 16793–16800.

Cantrell, C.A., Davidson, J.A., McDaniel, A.H., Shetter, R.E., Calvert, J.G., 1990. Temperature-dependent formaldehyde cross sections in the near-ultraviolet spectral region. Journal of Physical Chemistry 94, 3902–3908.

Carpenter, L.J., Monks, P.S., Bandy, B.J., Penkett, S.A., Galbally, I.E., Meyer, C.P.(Mick), 1997. A study of peroxy radicals and ozone photochemistry at coastal sites in the northern and southern hemispheres. Journal of Geophysical Research 102, 25417–25427.

Crawford, J., Davis, D., Chen, G., Shetter, R., Müller, M., Barrick, J., Olson, J., 1999. An assessment of cloud effects on photolysis rate coefficients: comparison of experimental and theoretical values. Journal of Geophysical Research 104, 5725–5734.

Daumont, D., Brion, J., Charbonnier, J., Malicet, J., 1992. Ozone UV Spectroscopy I: absorption cross-section at room temperature. Journal of Atmospheric Chemistry 15, 145–155.

DeMore, W., Howard, C., Sander, S., Ravishankara, A., Golden, D., Kolb, C., Hampson, R., Molina, M., Kurylo, M., 1997. Chemical kinetics and photochemical data for use in stratospheric modeling, evaluation number 12, NASA Jet Propulsion Laboratory, Pasadena, CA.

Elterman, L., 1968. UV, Visible, and IR Attenuation for Altitudes to 50 km; AFCRL-68-0153. Air Force Cambridge Res. Lab, Bedford, MA.

Erlick, C., Frederick, J.E., 1998. Effects of aerosols on the wavelength dependence of atmospheric transmission in the ultraviolet and visible. 2. Continental and urban aerosols in clear skies. Journal of Geophysical Research 103, 23275–23285.

Frederick, J.E., Erlick, C., 1997. The attenuation of sunlight by high-latitude clouds: spectral dependence and its physical mechanisms. Journal of Atmospheric Science 54, 2813–2819.

Früh, B., Trautmann, T., Wendisch, M., Keil, A., 2000. Comparison of observed and simulated NO_2 photodissociation frequencies in a cloudless atmosphere and in continental boundary layer clouds. Journal of Atmospheric Chemistry 105, 9843–9857.

Graham, R.A., Johnston, H.S., 1978. The photochemistry of NO_3 and the kinetics of the $N_2O_5 - O_3$ system. Journal of Physical Chemistry 82, 254–268.

Harder, J.W., Brault, J.W., Johnston, P.V., Mount, G.H., 1997. Temperature dependent NO_2 cross sections at high spectral resolution. Journal of Geophysical Research 102, 3861–3879.

Harwood, M.H., Burkholder, J.B., Hunter, M., Fox, R.W., Ravishankara, A.R., 1997. Absorption cross sections and self-reaction kinetics of the IO radical. Journal of Physical Chemistry 101, 853–863.

Harwood, M.H., Jones, R.L., 1994. Temperature dependent ultraviolet-visible absorption cross sections of NO_2 and N_2O_4: low-temperature measurements of the equilibrium constant for $2NO_2 \leftrightarrow N_2O_4$. Journal of Geophysical Research 99, 22955–22964.

Hofzumahaus, A., Kraus, A., Müller, M., 1999. Solar actinic flux spectroradiometry: a technique for measuring photolysis frequencies in the atmosphere. Applied Optics 38, 4443–4460.

Hofzumahaus, A., Kraus, A., Kylling, A., Zerefos, C.S., 2002. Solar actinic radiation (280–420 nm) in the cloud-freee troposphere between ground and 12 km altitude: measurements and model results. Journal of Geophysical Research 107 (D18), 8139 doi:10.1029/2001JD900142.

Hough, A.M., 1988. The calculation of photolysis rates for use in global tropospheric modelling studies. AERE Report R-13259 (HMSO), London.

Jacobson, M.Z., 1998. Studying the effects of aerosols on vertical photolysis rate coefficient and temperature profiles over an urban airshed. Journal of Geophysical Research 103, 10593–10604.

Jenkin, M.E., Saunders, S.M., Pilling, M.J., 1997. The tropospheric degradation of volatile organic compounds: a protocol for mechanism development. Atmospheric Environment 31, 81–104.

Junkermann, W., 1994. Measurements of the $J(O^1D)$ actinic flux within and above stratiform clouds and above snow surfaces. Geophysical Research Letters 21, 793–796.

Kanaya, Y., Matsumoto, J., Kato, S., Akimoto, H., 2001. Behavior of OH and HO_2 radicals during the Observations at a Remote Island of Okinawa (ORION99) field campaign: 2. Comparison between observations and calculations. Journal of Geophysical Research 106, 24209–24223.

Kanaya, Y., Yokouchi, Y., Matsumoto, J., Nakamura, K., Kato, S., Tanimoto, H., Furutani, H., Toyota, K., Akimoto, H., 2002. Implications of iodine chemistry for daytime HO_2 levels at Rishiri Island. Geophysical Research Letters 29(8), 10.1029/2001GL014061.

Kelley, P., Dickerson, R.R., Luke, W.T., Kok, G.L., 1995. Rate of NO_2 photolysis from the surface to 7.6 km altitude in clear-sky and clouds. Geophysical Research Letters 22, 2621–2624.

Kraus, A., Hofzumahaus, A., 1998. Field measurements of atmospheric photolysis frequencies for O_3, NO_2, HCHO,

CH_3CHO, H_2O_2, and HONO by UV spectroradiometry. Journal of Atmospheric Chemistry 31, 161–180.

Kraus, A., Rohrer, F., Hofzumahaus, A., 2000. Intercomparison of NO_2 photolysis frequency measurements by actinic flux spectroradiometry and chemical actinometry during JCOM97. Geophysical Research Letters 27, 1115–1118.

Lantz, K.O., Shetter, R.E., Cantrell, C.A., Flocke, S.J., Calvert, J.G., Madronich, S., 1996. Theoretical, actinometric, and radiometric determinations of the photolysis rate coefficient of NO_2 during the Mauna Loa Observatory Photochemistry Experiments 2. Journal of Geophysical Research 101, 14613–14629.

Liao, H., Yung, Y.L., Seinfeld, J.H., 1999. Effects of aerosols on tropospheric photolysis rates in clear and cloudy atmospheres. Journal of Geophysical Research 104, 23697–23707.

Madronich, S., Hastie, D.R., Ridley, B.A., Schiff, H.I., 1983. Measurement of the photodissociation coefficient of NO_2 in the atmosphere: i. method and surface measurements. Journal of Atmospheric Chemistry 1, 3–25.

Madronich, S., Flocke, S., 1998. The role of solar radiation in atmospheric chemistry. In: Boule, P. (Ed.), Handbook of Environmental Chemistry. Springer, Heidelberg, pp. 1–26.

Maric, D., Burrows, J.P., Moortgat, G.K., 1994. A study of the UV-visible absorption spectra of Br_2 and BrCl. Journal of Photochemistry and Photobiology A—Chemistry 83, 179–192.

McKenzie, R., Johnston, P., Hofzumahaus, A., Kraus, A., Madronich, S., Cantrell, C., Calvert, J., Shetter, R., 2002. Relationship between photolysis frequencies derived from spectroscopic measurements of actinic fluxes and irradiances during the IPMMI campaign. Journal of Geophysical Research 107 (D5), 10.1029/2001JD000601.

Mössinger, J.C., Shallcross, D.E., Cox, R.A., 1998. UV-VIS absorption cross sections and atmospheric lifetimes of CH_2Br_2, CH_2I_2, and CH_2BrI. Journal of the Chemical Society Faraday Transactions 94, 1391–1396.

Müller, M., Kraus, A., Hofzumahaus, A., 1995. $O_3 \rightarrow O(^1D)$ photolysis frequencies determined from spectroradiometric measurements of solar actinic UV-radiation: comparison with chemical actinometer measurements. Geophysical Research Letters 22, 679–682.

Passchier, A.A., Christian, J.D., Gregory, N.W., 1967. The ultraviolet-visible absorption spectrum of bromine between room temperature and 440 degree. Journal of Physical Chemistry 71, 937–942.

Payne, R.E., 1972. Albedo of the sea surface. Journal of Atmospheric Science 29, 959.

Platt, U., 2000. Reactive halogen species in the mid-latitude troposphere—Recent discoveries. Water, Air, and Soil Pollution 123, 229–244.

Roehl, C.M., Burkholder, J.B., Moortgat, G.K., Ravishankara, A.R., Crutzen, P.J., 1997. Temperature dependence of UV absorption cross sections and atmospheric implications of several alkyl iodides. Journal of Geophysical Research 102, 12819–12829.

Rowley, D.M., Mössinger, J.C., Cox, R.A., Jones, R.L., 1999. The UV-visible absorption cross-sections and atmospheric photolysis rate of HOI. Journal of Atmospheric Chemistry 34, 137–151.

Sander, S., P., Friedl, R.R., DeMore, W.B., Ravishankara, A.R., Golden, D.M., Kolb, C.E., Kurylo, M.J., Hampson, R.F., Huie, R.E., Molina, M.J., Mootgat, G.K., 2000. Chemical kinetics and photochemical data for use in stratospheric modeling, supplement to evaluation number 12: Update of key reactions, evaluation number 13, NASA Jet Propulsion Laboratory, Pasadena, CA.

Seckmeyer, G., Erb, R., Albold, A., 1996. Transmittance of a cloud is wavelength-dependent in the UV-range. Geophysical Research Letters 23, 2753–2755.

Seery, D.J., Britton, D., 1964. The continuous absorption spectra of chlorine, bromine, bromine chloride, iodine chloride, and iodine bromide. Journal of Physical Chemistry 68, 2263–2266.

Shetter, R.E., Müller, M., 1999. Photolysis frequency measurements using actinic flux spectroradiometry during the PEM-tropics mission: instrumentation description and some results. Journal of Geophysical Research 104, 5647–5661.

Shetter, R.E., et al., 1996. Actinometric and radiometric measurement and modeling of the photolysis rate coefficient of ozone to $O(^1D)$ during Mauna Loa Observatory Photochemistry Experiment 2. Journal of Geophysical Research 101, 14631–14641.

Talukdar, R.K., Burkholder, J.B., Schmoltner, A.-M., Roberts, J.M., Wilson, R.R., Ravishankara, A.R., 1995. Investigation of the loss processes for peroxyacetyl nitrate in the atmosphere: UV photolysis and reaction with OH. Journal of Geophysical Research 100, 14163–14173.

Tanimoto, H., Kajii, Y., Hirokawa, J., Akimoto, H., Minko, N.P., 2000. The atmospheric impact of boreal forest fires in far eastern Siberia on the seasonal variation of carbon monoxide: observations at Rishiri, a northern remote Island in Japan. Geophysical Research Letters 27, 4073–4076.

Tellinghuisen, J., 1973. Resolution of the visible-infrared absorption spectrum of I_2 into three contributing transitions. Journal of Chemical Physics 58, 2821–2834.

Torres, O., Bhartia, P.K., Herman, J.R., Sinyuk, A., Ginoux, P., Holben, B., 2002. A long-term record of aerosol optical depth from TOMS observations and comparison to AERONET measurements. Journal of Atmospheric Science 59, 398–413.

Vaghjiani, G.L., Ravishankara, A.R., 1989. Absorption cross sections of CH_3OOH, H_2O_2, and D_2O_2 vapors between 210 and 365 nm at 297 K. Journal of Geophysical Research 94, 3487–3492.

Volz-Thomas, A., Lerner, A., Pätz, H.-W., Schultz, M., McKenna, D.S., Schmitt, R., Madronich, S., Röth, E.P., 1996. Airborne measurements of the photolysis frequency of NO_2. Journal of Geophysical Research 101, 18613–18627.

Wahner, A., Ravishankara, A.R., Sander, S.P., Friedl, R.R., 1988. Absorption Cross Section of BrO between 312 and 385 nm at 298 and 223 K. Chemical Physics Letters 152, 507–512.